Characterization of the CVD Graphene Monolayer as an Active Element of a One-Port Microwave Device

Jarosław Judek, Mariusz Zdrojek, Jan Sobieski, Aleksandra Przewłoka, and Jerzy K. Piotrowski

***Abstract*— The one-port configuration of a microwave device is the simplest architecture for graphene ultrafast (photo-)resistors, (photo-)diodes, sensors, and photodetectors. Here, this configuration is realized by a segment of coplanar waveguide (CPW) loaded with a CVD graphene monolayer shorted to the ground. The magnitude and phase of the reflection coefficient (S_{11} parameter) measured in the 0.1 ÷ 26 GHz frequency range are presented for undisturbed structures as well as for structures illuminated by white light and electrostatically polarized with the backgate. A simple and robust de-embedding procedure based on the signal flow graph and allowing for a simultaneous extraction of the parameters characterizing the CPW segment and the graphene monolayer is proposed. The graphene impedance at microwave frequencies is in good agreement with the value of dc sheet resistance obtained from van der Pauw measurements. The back-gate voltage modulation is an efficient way to modulate both the dc sheet resistance and the impedance. In particular, the Dirac point can be achieved both at microwave frequencies and at dc. An equivalent circuit model consists of only the resistance and capacitance connected in parallel, because of good quality ohmic contacts and a negligible inductance as a result of low-current flow in high-resistance graphene samples.**

***Index Terms*— Graphene, microwaves, one-port device.**

I. Introduction

GRAPHENE grown through the chemical vapor deposition method (CVD) on large-scale substrates [1]–[3] is often considered an active element of various high-speed electron devices such as MOSFET transistors operating at radio frequencies [4], microwave optical mixers [5], or ultrafast infrared/visible photodetectors [6]. This predisposition for application in ultrafast optoelectronics results from high carrier mobility [7], high saturation velocity [8], tunability of the resistance, ambipolar transport, and an optical absorption that is constant over a wide spectral range [9], [10]. Additional advantage is the relatively low resistance in comparison to other 2-D crystals, e.g., MoS_2, which allows for achieving impedance matching (approximately 50 Ω) with relatively low aspect ratio values. However, the proper design of devices working at radio, microwave or terahertz frequencies requires at least specialized input–output circuitries that take into account the wavy nature of the guided electric signals and knowledge of the frequency dependence of the complex impedance $Z(f)$ characterizing the active element. The literature on the microwave properties of exfoliated and CVD graphene widely discusses the problem of graphene impedance and has even proposed reasonable equivalent circuit models; however, all considered devices have been realized in a two-port configuration [11]–[17]. Such a configuration is convenient for ultrafast graphene transistors that are three-terminal devices, but for graphene (photo-)resistors, (photo-)diodes, sensors, and ultrafast photodetectors [18], [19] which are typically two-terminal devices, a more natural choice is the one-port configuration, on which we focus in this paper.

II. Device Fabrication and Experimental Details

A schematic of the proposed device architecture is shown in Fig. 1(a). The input–output circuitry is realized as a 350-μm long segment of coplanar waveguide (CPW) with dimensions matching the microwave probe with a 150-μm pitch [an image of a structure during measurements is shown in Fig. 1(b)] and a characteristic impedance of approximately 50 Ω at 10 GHz (further details can be found in [20]). The graphene monolayer, grown on copper foil, transferred onto Si/SiO_2 substrate with the delamination method [21] and etched with oxygen plasma to form a 50 μm × 50 μm square film, is placed just behind the end of the middle metal strip. Such high flake dimensions were chosen intentionally to average the local inhomogeneities originating in still-immature graphene production technology. An SEM image of the active area is shown in Fig. 1(c), whereas a typical Raman spectrum

Manuscript received June 6, 2017; revised August 9, 2017; accepted August 17, 2017. Date of publication September 6, 2017; date of current version September 20, 2017. This work was supported by The National Center for Research and Development through the projects under Grant Graftech/NCBR/13/20/2013 and Grant Lider/180/L-6/14/NCBR/2015. The review of this paper was arranged by Editor M. M. Cahay. *(Corresponding author: Jarosław Judek.)*

J. Judek and M. Zdrojek are with the Faculty of Physics, Warsaw University of Technology, 00-662 Warsaw, Poland (e-mail: jerryj@if.pw.edu.pl).

J. Sobieski is with the Faculty of Physics, Warsaw University of Technology, 00-662 Warsaw, Poland, and also with the Institute of Electronic Materials Technology, 01-919 Warsaw, Poland.

A. Przewłoka is with the Institute of Electronic Materials Technology, 01-919 Warsaw, Poland.

J. K. Piotrowski is with the Institute of Microelectronics and Optoelectronics, Faculty of Electronics and Information Technology, Warsaw University of Technology, 00-662 Warsaw, Poland.

Color versions of one or more of the figures in this paper are available online at http://ieeexplore.ieee.org.

Digital Object Identifier 10.1109/TED.2017.2742942

0018-9383 © 2017 IEEE. Personal use is permitted, but republication/redistribution requires IEEE permission.
See http://www.ieee.org/publications_standards/publications/rights/index.html for more information.

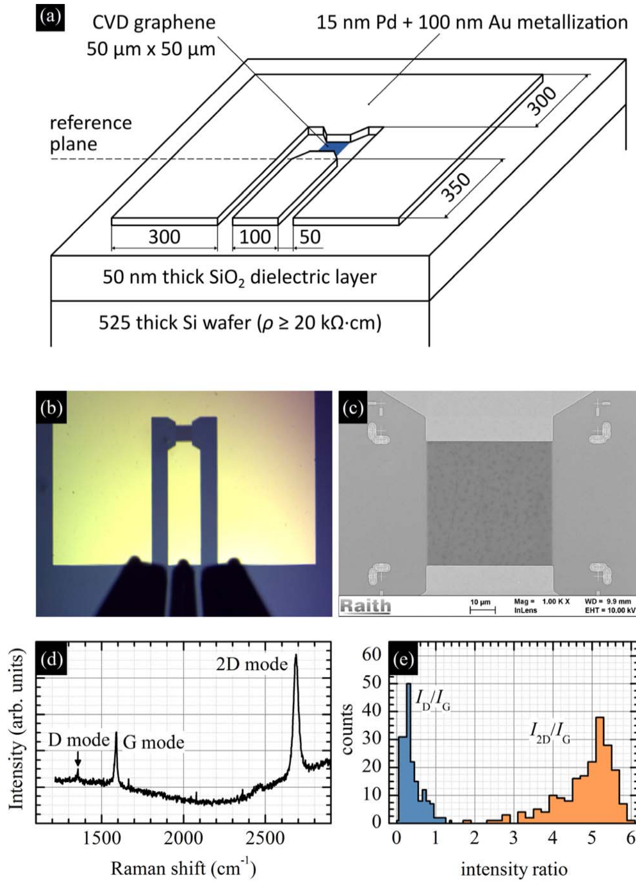

Fig. 1. (a) Schematic of the proposed device architecture—a segment of a CPW loaded with a CVD graphene monolayer shorted to the ground, all dimensions are in micrometers. (b) Image of the structure during microwave measurements using a ground-signal-ground probe. (c) SEM image of the 50 μm $\times$ 50 μm CVD graphene monolayer. (d) Typical Raman spectrum of graphene. (e) Distribution of the I_D/I_G ratio and the I_{2D}/I_G ratio.

is shown in Fig. 1(d). The positions, shapes, and intensities of D, G, and 2D Raman modes prove that the active area is made of graphene monolayer [22]. Fig. 1(e) shows the distributions of the ratio of the D mode intensity to the G mode intensity—I_D/I_G, and the distribution of the ratio of the 2D mode intensity to the G mode intensity—I_{2D}/I_G. Both can be treated as a measure of quality [23] and prove that after the device fabrication process the graphene is still of good quality. The one-port microwave structure ends with a transverse metal strip connected to the ground planes. For the substrate, we used high-resistivity silicon wafers (flat zone method, diameter 4," thickness 525 μm, orientation 100, boron doping, one side polished, $\rho \geq 20$ k$\Omega \cdot$ cm), which were thermally oxidized to produce a 50-nm-thick SiO_2 dielectric layer. Electron beam lithography followed by the lift-off process was used for fabrication of four sets of devices: 24 microwave one-port graphene structures, four four-probe graphene structures, four van der Pauw graphene structures, and four calibration structures without graphene for the de-embedding process. The metallization consisted of a 15-nm-thick Pd layer and a 100-nm-thick Au layer and was deposited by the resistive thermal evaporation technique under

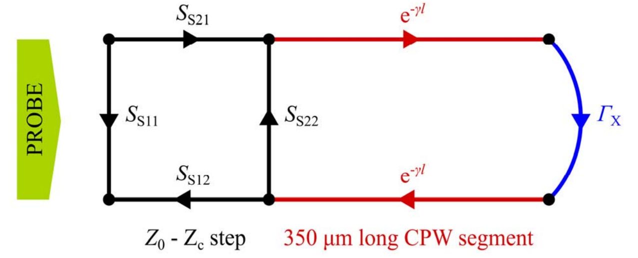

Fig. 2. Signal flow graph for a CPW segment with a Γ_X load at the end.

a pressure of 1×10^{-6} torr. The microwave measurements were performed as described in [20].

Extraction of the impedance of the graphene active area from raw data (here from S_{11} parameter) requires a de-embedding procedure adjusted to a particular architecture. In this paper, we propose a simple and robust procedure based on the signal flow graph illustrated in Fig. 2. The first element of the proposed signal flow graph is the $Z_0 - Z_C$ impedance step, which originates from the difference between the characteristic impedance of the probe, which equals $Z_0 = 50 + 0i\ \Omega$, and the frequency-dependent characteristic impedance of the CPW segment Z_C [24]. The second element is the waveguide characterized by the characteristic impedance Z_C and the complex propagation constant γ. The arbitrary load is characterized by the complex reflection coefficient Γ_X, which can be easily transformed into the complex impedance Z_X with the following equations:

$$\Gamma_X = \frac{S_{11} - S_{S11}}{1 - S_{11}S_{S11}} e^{2\gamma l}$$

where

$$S_{S11} = \frac{Z_c - Z_0}{Z_c + Z_0} \quad (1)$$

$$Z_X = Z_0 \cdot \frac{1 + S_{S11}}{1 - S_{S11}} \cdot \frac{1 + \Gamma_X}{1 - \Gamma_X}. \quad (2)$$

Calculation of the load impedance Z_X requires knowledge of three complex values: S_{11}, which can be directly measured, and S_{S11} and $e^{2\gamma l}$, which must be determined on additional calibration structures. In this paper, we used two calibration structures denoted *short* and *open*. The structures *short* and *open* are similar to the structure shown in Fig. 1(a) except that there is no graphene after the reference plane for the *open* structure, and there is an additional metallization between the reference plane and the transverse metal strip for the *short* structure. Our study on the reflection coefficient from *short* and *open* structures characterized by different metallization thickness (similar to the study described in [20], not published) showed that it is reasonable to assume that $\Gamma_{short} = -1$ and $\Gamma_{open} = +1$. We are aware that strict description of short structures requires additional inductance that corresponds to additional current flow in the transverse metal strip and the strict description of open structures requires additional capacitance that corresponds to the electric field that goes out the end of the central metal strip [25]–[27] but in our case these give corrections that are much below the occurring uncertainties originating in instrumental limitations and human-factor

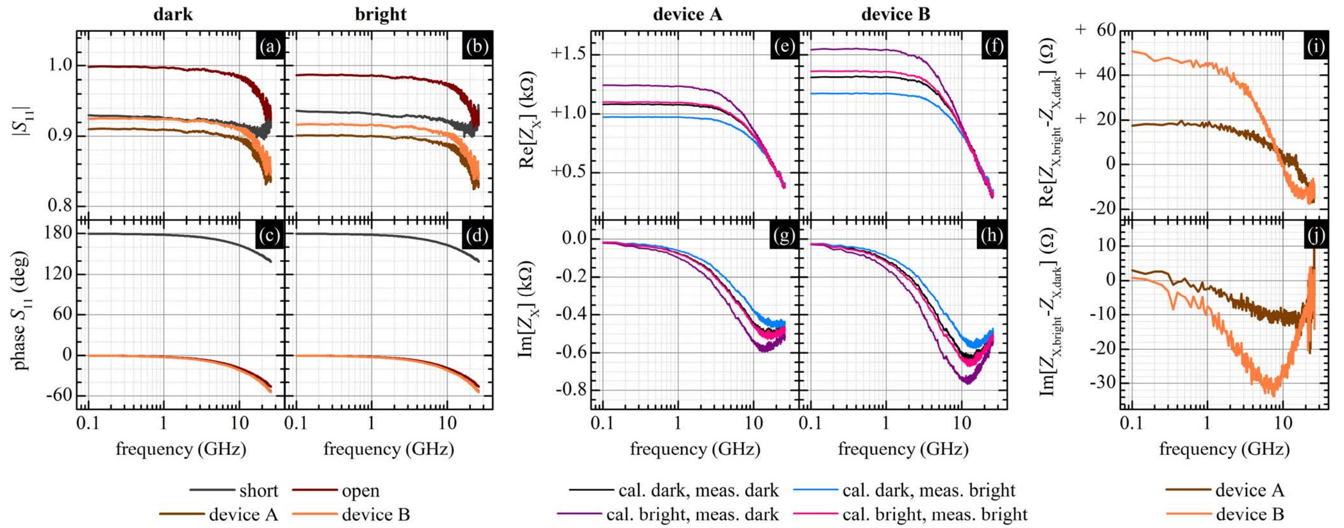

Fig. 3. Measured frequency characteristics (0.1 ÷ 26.1 GHz) of (a) and (b) magnitude and (c) and (d) phase of the reflectance S_{11} for structures (a) and (c) not illuminated and (b) and (d) illuminated with white light. Structures denoted *short* and *open* are used for the de-embedding procedure, structures denoted *device A* and *device B* are those of the graphene devices. Calculated frequency characteristics of the (e) and (f) real and (g) and (h) imaginary parts of the graphene impedance Z_X for *device A* and *device B*. Changes of the (i) real and (j) imaginary parts of the graphene impedance Z_X for *device A* and *device B* due to light illumination.

errors. In consequence, the complex value of S_{S11} and $e^{2\gamma l}$ can be found with the following equations:

$$\frac{S_{11,\text{short}} - S_{S11}}{1 - S_{11,\text{short}} S_{S11}} e^{2\gamma l} = -1 + 0i \quad (3)$$

$$\frac{S_{11,\text{open}} - S_{S11}}{1 - S_{11,\text{open}} S_{S11}} e^{2\gamma l} = +1 + 0i. \quad (4)$$

We note that obtained parameters characterizing the segment of waveguide using calibration structures are in agreement with results obtained in [20].

III. Experimental Results

Fig. 3(a)–(d) shows two sets of raw results for the microwave measurements on two graphene-based one-port structures (denoted *device A* and *device B*) and two calibration structures (denoted *short* and *open*). The first set of data was acquired without any light illumination, whereas the second set was acquired with white light illumination of the entire device structure. As shown, the light illumination affects the magnitudes of the reflectance for all structures, both with and without graphene. For example, at $f = 1$ GHz the magnitude of S_{11} parameter changes upon illumination from 0.998 to 0.987 for *open* structure, from 0.926 to 0.932 for *short* structure, from 0.910 to 0.901 for *device A*, and from 0.925 to 0.917 for *device B*. The changes in the S_{11} phase are of the order of 0.002°. Despite very little range of changes (with respect to the analyzer measurement uncertainties), the effect of light illumination is distinct, repeatable, reversible, and occurs on all structures with and without graphene. Observed changes result mostly from the changes in the carrier concentration in the high-resistivity silicon substrate, owing to the light absorption. An increase in the carrier concentration causes a decrease in the substrate resistivity, which increases microwave losses in the CPW, which is a well-known issue [28]–[37]. The properties of graphene active part are also influenced by the light illumination, but for our structures they are dominated by the changes in properties of the input–output circuitry. This aspect is very important because it might lead to incorrect conclusions in characterizing ultrafast graphene opto-electronic devices. To determine the possible consequences of a cursory approach to the analysis of light influence on microwave devices, we extracted the graphene impedance in four cases: #1 when both calibration and graphene structures were not illuminated; #2 when both calibration and graphene structures were illuminated; #3 when calibration structures were illuminated and graphene structures were not illuminated; and #4 when calibration structures were not illuminated and graphene structures were illuminated. The results are shown in Fig. 3(e)–(h). For cases #1 and #2, the results are close to each other, for case #3 the real part of the impedance is artificially inflated, and for case #4 it is understated. For example, at $f = 1$ GHz the real part of *device A* impedance equals 1078 Ω for case #1, 1095 Ω for case #2, 1232 Ω for case #3, and 971 Ω for case #4. For *device B* the real part of impedance equals 1309 Ω for case #1, 1353 Ω for case #2, 1543 Ω for case #3, and 1170 Ω for case #4. The case #4 is most important because it might lead to the false conclusion that the light absorption decreases the resistance of graphene active area due to the significant photogeneration of electron-hole pairs (change in R_S from 1078 Ω to 971 Ω, which is approximately −10% for *device A*, and change in R_S from 1309 Ω to 1170 Ω, which is approximately. −11% for *device B*), whereas the resistance indeed increases due to bolometric effect (change in change in R_S from 1078 Ω to 1095 Ω, which is approximately +1.6% for *device A*, and change in R_S from 1309 Ω to 1353 Ω which is approximately +3.4% for *device B*) [38], [39]. Fig. 3(i) and (j) illustrates true contribution of the light absorption in the graphene active area to the impedance change. As can be seen, the increase in resistance is of the order of tens of Ohm and decreases with frequency. All further measurements were performed without light illumination.

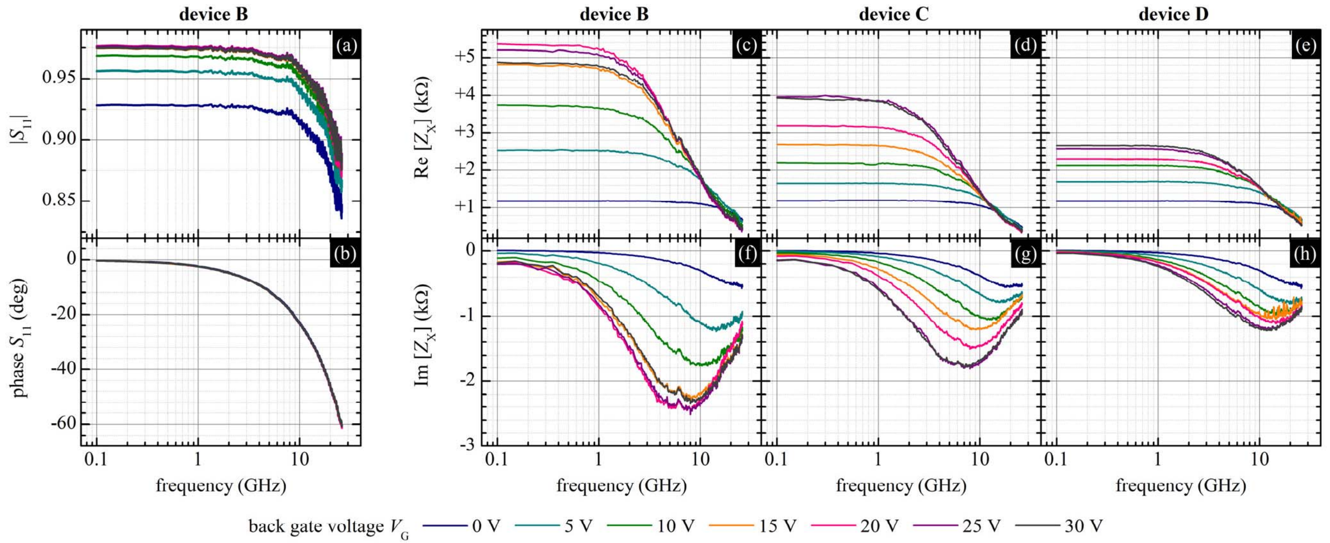

Fig. 4. Measured frequency characteristics (0.1 ÷ 26.1 GHz) of (a) magnitude and (b) phase of the reflectance S_{11} for the structure denoted *device B* as a function of the back-gate voltage. Calculated frequency characteristics of the (c)–(e) real and (f)–(h) imaginary parts of the graphene impedance Z_X for *device B*, *device C*, and *device D*. These devices have the same architecture, and the differences result from inhomogeneous graphene properties at the millimeter scale.

Fig. 4 presents data for structures electrostatically polarized by the backgate (we applied constant voltage to the substrate with respect to the grounded planes of CPW). Fig. 4(a) shows that the magnitude of the reflectance strongly depends on the back-gate potential, whereas the phase illustrated in Fig. 4(b) is almost constant. Because our internal study showed that the properties of the CPW are unaffected under back-gate modulation, we simply extracted the impedance of the graphene. Fig. 4(c)–(h) represents the real and imaginary parts of the impedance of the graphene active area for three different devices. These devices have the same architecture, and the differences result from inhomogeneous graphene properties at the millimeter scale. For all devices, the real part of the impedance increases with increased back-gate potential up to the Dirac point, and then it decreases. This trend is especially apparent for *device B*, which has the highest resistance for $V_{\mathrm{BG}} = 20$ V (Dirac point), whereas for $V_{\mathrm{BG}} = 25$ V, the resistance decreases, and for $V_{\mathrm{BG}} = 30$ V, it decreases even more. For *device C*, the resistance is equal for $V_{\mathrm{BG}} = 25$ V and $V_{\mathrm{BG}} = 30$ V with no further decrease. For *device D* the resistance does not reach its maximum in considered back-gate voltage range meaning that $V_{\mathrm{D}} > 40$ V. To better illustrate the influence of the back-gate voltage on the reflectance, the S_{11} magnitude and phase as a function of gate voltage are plotted for a fixed frequency $f = 1$ GHz in Fig. 5(a) and (b). When Fermi level in graphene approaches Dirac point the magnitude of reflectance reaches its maximum [Fig. 5(a)], when $V_{\mathrm{BG}} > V_{\mathrm{D}}$ the $|S_{11}|$ value decreases. It is a expected behavior resulting from the changes in the real part of the impedance Z_X, which at Dirac point reaches its maximum [Fig. 5(c)]. We note that while $|S_{11}|$ changes from 0.928 to 0.976 the resistance changes from 1.2 to 5.2 kΩ; and $R_X(V_{\mathrm{BG}} = V_{\mathrm{D}})/R_X(V_{\mathrm{BG}} = 0) = 4.4$. For *device C*, the Fermi level approaches Dirac point at $V_{\mathrm{BG}} = 25$ V and $R_X(V_{\mathrm{BG}} = V_{\mathrm{D}})/R_X(V_{\mathrm{BG}} = 0) = 3.2$. For *device D* the Fermi level never approaches Dirac point. At this point one comment should be done. The results of the S_{11} parameter measurements strongly depend on the conditions under which measurements are done including: history of the measurements and time of individual measurement (hysteresis). For instance, first measurement on *device B* gives result presented in Fig. 5(a)–(d), whereas next measurement performed just after the first one gives results similar to the one obtained for *device D*. Because during our measurements we changed the back-gate voltage from 0 to 30 V, the Dirac point was moving to even higher voltage values at each measurement. This prevented us from acquiring more results for lower change in back-gate voltage (e.g., 1 V instead of 5 V), because in such situation we never observed lowering of the reflectance with an increasing back-gate voltage. We note that all oberved effects are similar to effects observed for dc, which will be discussed in the following.

Fig. 4(c)–(h) also shows that the minimal value of the imaginary part of the impedance is closely related to the maximal value of the real part of the impedance, because the equivalent circuit model for such resistive samples consists of resistance R and capacitance C connected in parallel. The parallel capacitance ranges from 4 to 6 fF and slightly depends on the back-gate voltage. We note that at 10 GHz, $|Z_{C=5\ \mathrm{fF}}| \approx 3$ kΩ, a value comparable to the resistance. Approaching the Dirac point also has a consequence related to the decreasing bandwidth, which is related purely to the increase in the RC constant. We note that tuning the dimensions of the graphene active area (increase in width, decrease in the channel length) might change the equivalent circuit model to resistance and inductance connected in series, thus reducing the bandwidth decrease.

IV. DC Measurements

The last problem discussed in this paper is the correlation between dc and microwave measurements. For this purpose, we measured the graphene sheet resistance as a

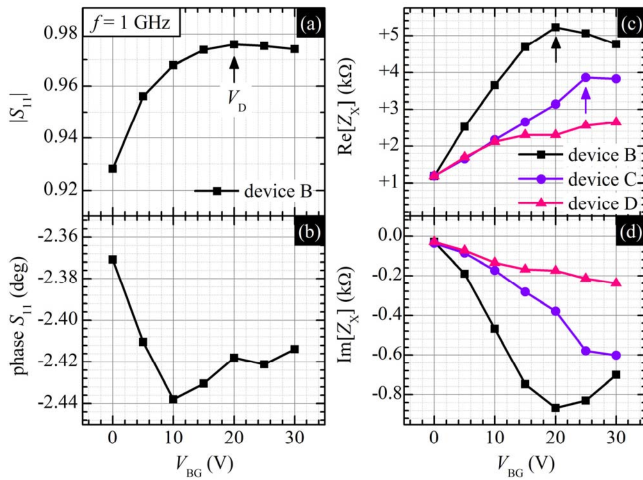

Fig. 5. Measured (a) magnitude and (b) phase of the reflectance S_{11} for the structure denoted *device B* as a function of the back-gate voltage at $f = 1$ GHz. Calculated (c) real and (d) imaginary parts of the graphene impedance Z_X for *device B*, *device C*, and *device D*. Arrows indicate Dirac points.

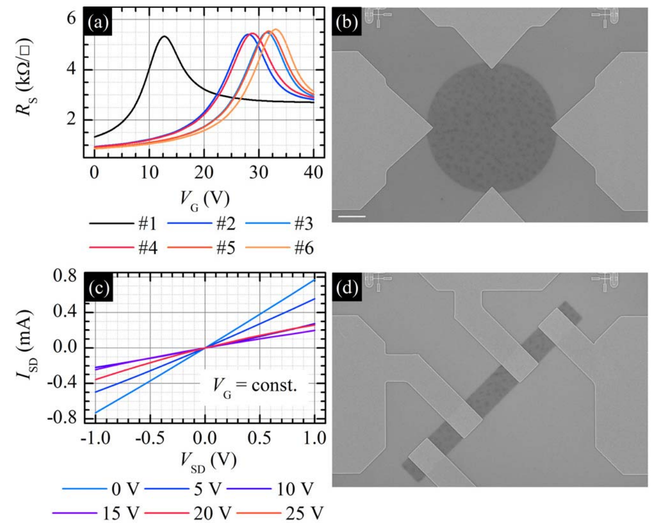

Fig. 6. (a) Graphene sheet resistance R_S versus back-gate voltage V_G, all measurements denoted #1 to #6 were performed sequentially, except #4 which was acquired a few minutes after #3. (b) SEM image of the van der Pauw structure, the length of the white bar equals 10 μm. (c) I–V characteristics taken from an FET-like graphene structure at different back-gate voltages. (d) SEM image of the four-probe structure.

function of the back-gate voltage by using the van der Pauw technique [40]. The results are shown in Fig. 6(a), whereas the SEM image of the fabricated structure is presented in Fig. 6(b). It can be seen that the dependence of the graphene sheet resistance on the gate voltage is sensitive to the history of the measurements, which is a known issue for graphene devices. Shift of the voltage at which resistance reaches its maximum value (Dirac point) in consecutive measurements results from charge trapping at the graphene/SiO_2 interface, in bulk SiO_2, on the SiO_2/Si interface, and/or by molecules adsorbed on the graphene surface [41]–[44]. As noticed by Carrion *et al.* [45] "trapping at the interfaces or within the bulk of the dielectrics surrounding the graphene channel is an inherent and challenging problem. Similar threshold voltage instabilities had also been observed in the early years of silicon technology and as recently as the last decade with the introduction of high-κ dielectrics and metal gate-stacks" [45]. This phenomenon is also why we cannot directly compare the dc and microwave back-gate voltage dependencies despite good qualitative agreement. Fig. 6(c) presents the I–V characteristics taken from an FET-like graphene structure at different back-gate voltages. The linear dependence of the current on the voltage verifies the ohmic nature of the fabricated contacts. Graphene structures like the one shown in Fig. 6(d) were used to estimate the contact resistance. The extracted values of R_C were below the uncertainty limit, thus demonstrating that metal/graphene contacts can be neglected. The low value of R_C results from a palladium buffer layer, which is believed to create the best contact to graphene [46]–[48].

V. Summary

In summary, we proposed and characterized a one-port graphene device architecture on a high-resistivity silicon substrate. We demonstrated that a cursory approach to the analysis of the light influence on a microwave device may lead to incorrect conclusions regarding the properties of optoelectronic devices. We also demonstrated that the graphene microwave impedance can be tuned by the back-gate voltage modulation as efficiently as the dc sheet resistance. Moreover, for a highly resistive active element, parallel capacitance can shorten the device to the ground and a good quality palladium/gold metallization allows for neglecting serial contact resistance. We note that our study is not limited to graphene but could be applicable to any other devices based on 2-D materials and thin films.

References

[1] A. Reina *et al.*, "Large area, few-layer graphene films on arbitrary substrates by chemical vapor deposition," *Nano Lett.*, vol. 9, no. 1, pp. 30–35, Dec. 2008.

[2] X. Li *et al.*, "Large-area synthesis of high-quality and uniform graphene films on copper foils," *Science*, vol. 324, no. 5932, pp. 1312–1314, Jun. 2009.

[3] Z. Yan, Z. Peng, and J. M. Tour, "Chemical vapor deposition of graphene single crystals," *Accounts Chem. Res.*, vol. 47, no. 4, pp. 1327–1337, Feb. 2014.

[4] Y. Wu *et al.*, "200 GHz maximum oscillation frequency in CVD graphene radio frequency transistors," *ACS Appl. Mater. Interfaces*, vol. 8, no. 39, pp. 25645–25649, Sep. 2016.

[5] A. Montanaro *et al.*, "Thirty gigahertz optoelectronic mixing in chemical vapor deposited graphene," *Nano Lett.*, vol. 16, no. 5, pp. 2988–2993, Apr. 2016.

[6] S. Schuler *et al.*, "Controlled generation of a p–n junction in a waveguide integrated graphene photodetector," *Nano Lett.*, vol. 16, no. 11, pp. 7107–7112, Oct. 2016.

[7] K. I. Bolotin *et al.*, "Ultrahigh electron mobility in suspended graphene," *Solid State Commun.*, vol. 146, pp. 351–355, Jun. 2008.

[8] I. Meric, M. Y. Han, A. F. Young, B. Ozyilmaz, P. Kim, and K. L. Shepard, "Current saturation in zero-bandgap, top-gated graphene field-effect transistors," *Nature Nanotechnol.*, vol. 3, no. 11, pp. 654–659, Sep. 2008.

[9] R. R. Nair *et al.*, "Fine structure constant defines visual transparency of graphene," *Science*, vol. 320, no. 5881, p. 1308, Jun. 2008.

[10] K. F. Mak, L. Ju, F. Wang, and T. F. Heinz, "Optical spectroscopy of graphene: From the far infrared to the ultraviolet," *Solid State Commun.*, vol. 152, pp. 1341–1349, Apr. 2012.

[11] S. Moon *et al.*, "Intrinsic high-frequency characteristics of graphene layers," *New J. Phys.*, vol. 12, pp. 113031–113040, Nov. 2010.

[12] H.-J. Lee, E. Kim, and J. Jung, "High frequency transmission properties of graphene monolayer with different coplanar waveguide electrode configurations," in *Proc. IEEE Nanotechnol. Mater. Devices Conf.*, Jeju, South Korea, Oct. 2011, pp. 313–314.

[13] N. Rouhi, D. Jain, S. Capdevila, L. Jofre, E. Brown, and P. J. Burke, "Broadband conductivity of graphene from DC to THz," in *Proc. 11th IEEE Int. Conf. Nanotechnol.*, Portland, OR, USA, Aug. 2011, pp. 1205–1207.

[14] H. S. Skulason *et al.*, "110 GHz measurement of large-area graphene integrated in low-loss microwave structures," *Appl. Phys. Lett.*, vol. 99, p. 153504, Oct. 2011.

[15] H.-J. Lee, E. Kim, J.-G. Yook, and J. Jung, "Intrinsic characteristics of transmission line of graphenes at microwave frequencies," *Appl. Phys. Lett.*, vol. 100, p. 223102, May 2012.

[16] M. Tuo *et al.*, "Nonlinear microwave characterization of CVD grown graphene," *IEEE Antennas Wireless Propag. Lett.*, vol. 15, pp. 1557–1560, Jan. 2016.

[17] S. A. Awan *et al.*, "Transport conductivity of graphene at RF and microwave frequencies," *2D Mater.*, vol. 3, no. 1, p. 015010, Feb. 2016.

[18] F. Xia, T. Mueller, Y. Lin, A. Valdes-Garcia, and P. Avouris, "Ultrafast graphene photodetector," *Nature Nanotechnol.*, vol. 4, no. 12, pp. 839–843, Oct. 2009.

[19] T. Mueller, F. Xia, and P. Avouris, "Graphene photodetectors for high-speed optical communications," *Nature Photon.*, vol. 4, pp. 297–301, Mar. 2010.

[20] J. Judek, A. P. Gertych, M. Świniarski, M. Zdrojek, J. Krupka, and J. K. Piotrowski, "Characterization of finite-width ground coplanar waveguides on high resistivity silicon with ultralow metallization thickness," *IEEE Trans. Microw. Theory Techn.*, doi: 10.1109/TMTT.2017.2731954.

[21] T. Ciuk *et al.*, "Properties of chemical vapor deposition graphene transferred by high-speed electrochemical delamination," *J. Phys. Chem. C*, vol. 117, no. 40, pp. 20833–20837, Sep. 2013.

[22] A. C. Ferrari *et al.*, "Raman spectrum of graphene and graphene layers," *Phys. Rev. Lett.*, vol. 97, no. 18, p. 187401, Nov. 2006.

[23] A. C. Ferrari, "Raman spectroscopy of graphene and graphite: Disorder, electron–phonon coupling, doping and nonadiabatic effects," *Solid State Commun.*, vol. 143, pp. 47–57, Jul. 2007.

[24] D. C. DeGroot, D. K. Walker, and R. B. Marks, "Impedance mismatch effects on propagation constant measurements," in *IEEE 5th Topical Meet., Elect. Perform. Electron. Packag. Dig.*, Dec. 1996, pp. 141–143.

[25] R. N. Simons and G. E. Ponchak, "Modeling of some coplanar waveguide discontinuities," *IEEE Trans. Microw. Theory Techn.*, vol. MTT-36, no. 12, pp. 1796–1803, Dec. 1988.

[26] K. Beilenhoff, H. Klingbeil, W. Heinrich, and H. L. Hartnagel, "Open and short circuits in coplanar MMIC's," *IEEE Trans. Microw. Theory Techn.*, vol. 41, no. 9, pp. 1534–1537, Sep. 1993.

[27] K. Beilenhoff, W. Heinrich, and H. L. Hartnagel, "Finite-difference analysis of open and short circuits in coplanar MMICs including finite metallization thickness and mode conversion," in *IEEE MTT-S Int. Microw. Symp. Dig.*, vol. 1. Albuquerque, NM, USA, Jun. 1992, pp. 103–106.

[28] W. Platte and B. Sauerer, "Optically CW-induced losses in semiconductor coplanar waveguides," *IEEE Trans. Microw. Theory Techn.*, vol. 37, no. 1, pp. 139–149, Jan. 1989.

[29] A. J. Seeds and A. A. A. de Salles, "Optical control of microwave semiconductor devices," *IEEE Trans. Microw. Theory Techn.*, vol. MTT-38, no. 5, pp. 577–585, May 1990.

[30] S. E. Saddow, B. J. Thedrez, S.-L. L. Huang, T. J. Mermagen, and C. H. Lee, "Investigation of the temperature and electric field dependence of a GaAs microwave photoconductive switch," in *Proc. SPIE, Optically Activated Switching III*, vol. 1873. Jun. 1993, pp. 89–96. [Online]. Available: http://dx.doi.org/10.1117/12.146555, doi: 10.1117/12.146555.

[31] S. E. Saddow and C. H. Lee, "Scattering parameter measurements on an optoelectronic attenuator," in *IEEE MTT-S Int. Microw. Symp. Dig.*, vol. 3. May 1994, pp. 1383–1386.

[32] S. E. Saddow, B. J. Thedrez, and C. H. Lee, "An optoelectronic attenuator for the control of microwave circuits," *IEEE Microw. Guided Wave Lett.*, vol. 3, no. 10, pp. 361–362, Oct. 1993.

[33] S. E. Saddow and C. H. Lee, "Optical control of microwave-integrated circuits using high-speed GaAs and Si photoconductive switches," *IEEE Trans. Microw. Theory Techn.*, vol. 43, no. 9, pp. 2414–2420, Sep. 1995.

[34] N. A. Riza and S. E. Saddow, "Optically controlled photoconductive N-bit switched microwave signal attenuator," *IEEE Microw. Guided Wave Lett.*, vol. 5, no. 12, pp. 448–450, Dec. 1995.

[35] J. R. Flemish, H. W. Kwan, R. L. Haupt, and M. Lanagan, "A new silicon-based photoconductive microwave switch," *Microw. Opt. Technol. Lett.*, vol. 51, pp. 248–252, Jan. 2009.

[36] J. R. Flemish and R. L. Haupt, "Optimization of a photonically controlled microwave switch and attenuator," *IEEE Trans. Microw. Theory Techn.*, vol. 58, no. 10, pp. 2582–2588, Oct. 2010.

[37] K. B. Ali, C. R. Neve, A. Gharsallah, and J.-P. Raskin, "Photo-induced coplanar waveguide RF switch and optical crosstalk on high-resistivity silicon trap-rich passivated substrate," *IEEE Trans. Electron Devices*, vol. 60, no. 10, pp. 3478–3484, Oct. 2013.

[38] D. K. Efetov and P. Kim, "Controlling electron-phonon interactions in graphene at ultrahigh carrier densities," *Phys. Rev. Lett.*, vol. 105, no. 25, p. 256805, 2010.

[39] M. Freitag, T. Low, F. Xia, and P. Avouris, "Photoconductivity of biased graphene," *Nature Photon.*, vol. 7, pp. 53–59, Dec. 2012.

[40] L. J. van der Pauw, "A method of measuring specific resistivity and Hall effect of disks of arbitrary shape," *Philips Res. Rep.*, vol. 13, pp. 1–9, Feb. 1958.

[41] P. Joshi, H. E. Romero, A. T. Neal, V. K. Toutam, and S. A. Tadigadapa, "Intrinsic doping and gate hysteresis in graphene field effect devices fabricated on SiO_2 substrates," *J. Phys., Condens. Matter*, vol. 22, p. 334214, Aug. 2010.

[42] H. Wang, Y. Wu, C. Cong, J. Shang, and T. Yu, "Hysteresis of electronic transport in graphene transistors," *ACS Nano*, vol. 4, no. 12, pp. 7221–7228, 2010.

[43] Y. G. Lee *et al.*, "Fast transient charging at the graphene/SiO_2 interface causing hysteretic device characteristics," *App. Phys. Lett.*, vol. 98, p. 183508, May 2011.

[44] Y. G. Lee *et al.*, "Influence of extrinsic factors on accuracy of mobility extraction in graphene metal-oxide-semiconductor field effect transistors," *Appl. Phys. Lett.*, vol. 102, p. 093121, Mar. 2013.

[45] E. A. Carrion *et al.*, "Hysteresis-free nanosecond pulsed electrical characterization of top-gated graphene transistors," *IEEE Trans. Electron Devices*, vol. 61, no. 5, pp. 1583–1589, May 2014.

[46] F. Xia, V. Perebeinos, Y.-M. Lin, Y. Wu, and P. Avouris, "The origins and limits of metal–graphene junction resistance," *Nature Nanotechnol.*, vol. 6, pp. 179–184, Feb. 2010.

[47] H. Zhong *et al.*, "Realization of low contact resistance close to theoretical limit in graphene transistors," *Nano Res.*, vol. 8, no. 5, pp. 1669–1679, May 2015.

[48] Q. Wilmart *et al.*, "Contact gating at GHz frequency in graphene," *Sci. Rep.*, vol. 6, Feb. 2016, Art. no. 21085.

Authors' photographs and biographies not available at the time of publication.